Heliyon 10 (2024) e35793

Contents lists available at ScienceDirect

Heliyon

journal homepage: www.cell.com/heliyon

Research article

Combined bacterial translocation and cholestasis aggravates liver injury by activation pyroptosis in obstructive jaundice

Xin Shen [a,1], Xin Zhang [b,1], Kaiyu Li [c], Guangming Huang [c], Xinyu Li [c], Yunlong Hou [d], Xin Ge [c,*]

[a] Department of Pharmacy, National Cancer Center/National Clinical Research Center for Cancer/Cancer Hospital, Chinese Academy of Medical Sciences and Peking Union Medical College, Beijing, 100021, China
[b] Luoyang Orthopedic-Traumatological Hospital of Henan Province (Henan Provincial Orthopedic Hospital), Luoyang, 471002, Henan, China
[c] Department of General Surgery, Heilongjiang Provincial Hospital, 82 Zhongshan Road, Harbin, 150036, Heilongjiang, China
[d] National Key Laboratory of Collateral Disease Research and Innovative Chinese Medicine, Shijiazhuang, 050000, Hebei, China

ARTICLE INFO

Keywords:
Obstructive jaundice
Intestinal bacterial translocation
Pyroptosis
Inflammasome
Liver injury

ABSTRACT

This study explores the mechanism by which obstructive jaundice (OJ) induces liver damage through pyroptosis. We induced OJ in rats via bile duct ligation and assessed liver damage using serum biochemical markers and histological analysis of liver tissue. Pyroptosis was investigated through immunofluorescence, ELISA, Western blot, and quantitative RT-PCR techniques. Additionally, we examined intestinal function and fecal microbiota alterations in the rats using 16S rDNA sequencing. In vitro experiments involved co-culturing Kupffer cells and hepatocytes, which were then exposed to bile and lipopolysaccharide (LPS). Our findings indicated that OJ modified the gut microbiota, increasing LPS levels, which, in conjunction with bile, initiated a cycle of inflammation, fibrosis, and cell death in the liver. Mechanistically, OJ elevated necrotic markers such as ATP, which in turn activated pyroptotic pathways. Increased levels of pyroptosis-related molecules, including NLRP3, caspase-1, gasdermin D, and IL-18, were confirmed. In our co-cultured cell model, bile exposure resulted in cell death and ATP release, leading to the activation of the NLRP3 inflammasome and its downstream effectors, caspase-1 and IL-18. The combination of bile and LPS significantly intensified pyroptotic responses. This study is the first to demonstrate that LPS and bile synergistically exacerbate liver injury by promoting necrosis and pyroptosis, unveiling a novel mechanism of OJ-associated hepatic damage and suggesting avenues for potential preventive or therapeutic interventions.

1. Introduction

Obstructive jaundice (OJ) results from impaired bile flow into the intestine, frequently observed in surgical patients and commonly associated with gallstones, malignant tumors, and various other pathological states [1]. This disorder manifests through a spectrum of clinical symptoms including jaundice, discolored urine, pale stools, pruritus, malabsorption, and cholangitis, along with liver and renal dysfunction [2]. These symptoms indicate extensive pathophysiological changes across multiple organ systems. A critical complication

* Corresponding author.
E-mail address: gexin628@163.com (X. Ge).
[1] Both authors contribute equally.

https://doi.org/10.1016/j.heliyon.2024.e35793
Received 2 February 2024; Received in revised form 2 August 2024; Accepted 2 August 2024
Available online 3 August 2024

Abbreviations

ALT	Alanine transaminase
ALP	Alkaline phosphatase
AST	Aspartate transaminase
BDL	Bile duct ligation
cGMP	Cyclic guanosine monophosphate
DAO	Diamine oxidase
DBIL	Direct bilirubin
H&E	Hematoxylin and eosin
IF	Immunofluorescent staining
LPS	Lipopolysaccharide
OJ	Obstructive jaundice
PAS	Periodic acid-Schiff
PCoA	Principal coordinate analysis
SIgA	Secretory immunoglobulin A
TBA	Total bile acids
TBIL	Total bilirubin

of OJ is the accumulation of bile acids in the liver, a condition known as cholestasis. This accumulation can lead to hepatotoxicity, promoting the death of hepatocytes and triggers inflammatory responses [3]. These processes may progress to hepatic fibrosis and, eventually, liver failure [4]. Despite considerable research into the mechanisms underlying cholestasis, the specific pathogenetic pathways of cholestatic liver injury remain poorly understood, highlighting a significant gap in effective preventive strategies.

Growing evidence underscores the critical role of macrophage pyroptosis in the pathogenesis of liver injury [5]. Pyroptosis is a form of programmed cell death pathway involving necrosis and apoptosis, primarily observed in macrophages and driven by inflammation [6]. This cell death pathway is regulated by inflammasomes, which activate under conditions such as bacterial infections, where caspase-1 facilitates pyroptosis in macrophages and dendritic cells [7]. During pyroptosis, affected cells rapidly secrete proinflammatory cytokines, particularly IL-1β and IL-18, which can trigger both localized and systemic inflammatory responses [8]. Kupffer cells, specialized macrophages in the liver, play a crucial role in maintaining liver homeostasis by clearing foreign particles or red blood cells from the circulation through phagocytosis. Several studies have investigated the relationship between Kupffer cells and pyroptosis. Evidence suggests that liver ischemia-reperfusion can initiate pyroptosis through the guanylate-cyclase (sGC)-cyclic guanosine monophosphate (cGMP) signal pathway [9], and lipopolysaccharide (LPS) can induce pyroptosis in Kupffer cells via interaction with GPR120 and NLRP3 [10]. Despite these insights, the specific role of Kupffer cell pyroptosis in cholestatic liver injury remains unclear, marking a significant gap in our understanding of cholestasis pathophysiology.

In recent years, there has been an increasing focus on studying gut microbiota, often referred to as a "microbial organ" due to its significant impact on host health through symbiotic interactions. This microbial community plays a crucial role in various physiological processes, including nutrient digestion and absorption, immune system development, and protection against pathogens [11–13]. A balanced intestinal microflora offers numerous advantages to the host, such as pathogen exclusion, enhancement of intestinal barrier integrity, facilitation of normal nutrient digestion and absorption, and promotion of other beneficial microorganisms [14]. However, alteration of gut microbiota can impair the intestinal barrier, contributing to bacterial translocation [15]. The liver, as the initial organ to encounter xenobiotics after their absorption from the intestine, plays a significant role in biotransformation and metabolism [16]. Prior experimental investigations have shown that OJ induces morphological changes in the intestinal mucosa, indicative of atrophy, along with increased crypt epithelial apoptosis and intestinal oxidative stress [17–19]. Notably, disruption of the intestinal barrier has been observed in both rodent models of cholestatic liver diseases induced by bile duct ligation (BDL) and o in OJ patients [20]. Recent clinical investigations have further demonstrated that dysfunction of the intestinal barrier and subsequent bacterial translocation play significant roles in the progression of cholestatic liver diseases [21]. Thus, the occurrence of intestinal injury emerges as a crucial element in the pathophysiology of gut barrier dysfunction in OJ [22]. However, there is still a lack of relevant experimental research on whether dysbiosis-induced disruption of the intestinal barrier and subsequent activation of intestinal bacteria and their metabolites mediate Kupffer cell pyroptosis, leading to cholestatic liver injury.

In this study, we hypothesized that dysbiosis-induced disruption of the intestinal barrier exacerbates cholestatic liver injury. To investigate this, we utilized a rat model of obstructive jaundice (OJ) induced by bile duct ligation (BDL). Using 16S rDNA sequencing, we established a link between OJ-induced dysbiosis and the compromise of the intestinal barrier, confirming the translocation of intestinal flora to the liver. Subsequent analyses revealed that ensuing cholestasis and translocation of lipopolysaccharide (LPS) to the liver initiated inflammatory processes that further intensified liver injury. These investigations provide new insights into the complex pathophysiological mechanisms underlying OJ.

2. Methods

2.1. Experimental animals

Sixteen male Sprague-Dawley rats, aged 8 weeks and weighing between 300 and 350 g, were accommodated in a controlled environment with a 12-h light/dark cycle and a constant temperature of 23 ± 2 °C. These rats were had unrestricted access to food and water. The animal experiments were approved by the Animal Care and Use Committee of the Medical Research Institute of Yiling (NO. N2022014) and conducted in adherence to the guidelines outlined in the Principles of Laboratory Animal Care and the Guide for the Care and the Guide for the Care and Use of Laboratory Animals. All research was conducted in accordance with both the Declarations of Helsinki and Istanbul.

The bile duct ligation (BDL) surgical technique was performed under general anesthesia using intramuscular administration of pentobarbital sodium (18 mg/kg), as described in a prior publication [23] (Fig. 1). A control group of Sham rats underwent a similar procedure, except for BDL. Assessments were conducted 7 days post-surgery.

2.2. Serum biochemical analysis

The biochemical markers examined in this study included serum alanine transaminase (ALT), serum aspartate transaminase (AST), serum total bilirubin (TBIL), serum direct bilirubin (DBIL), serum alkaline phosphatase (ALP), serum total bile acids (TBA), and serum diamine oxidase (DAO). Serum levels of ALT, AST, TBIL, DBIL, and ALP were measured using an automatic blood biochemical analyzer (ADVIA2400, Siemens, USA). The serum TBA concentration was determined using TBA kits (E003-2-1, Nanjing Jiancheng Bioengineering Institute, China). Additionally, serum DAO activity was assessed using a DAO assay kit (BC1285, Solarbio, China).

2.3. Histopathological examination

The fixed tissues underwent dehydration using a series of alcohol gradients and then embedded in paraffin blocks. Tissue sections with a thickness of 5 μm were subsequently prepared and mounted onto slides. The liver tissue and small intestine were subjected to histopathological evaluation under a microscope after staining with hematoxylin and eosin (H&E). Additionally, liver fibrosis was assessed using Masson-stained sections, in accordance with the instructions provided by the manufacturer. The presence of blue coloration on the Masson's trichrome-stained tissue indicates the presence of scar tissue.

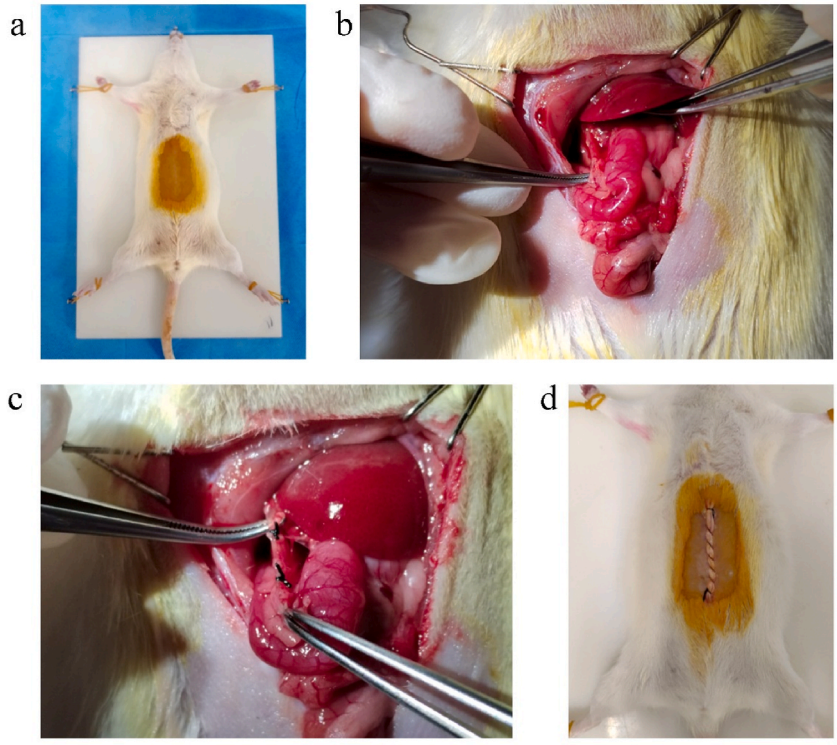

Fig. 1. Surgical procedure of BDL. (a) The necessary steps for the surgical procedure included anesthesia administration, fixation of the rats, skin preparation, and disinfection. (b) The dissection process was performed to expose the common bile duct. (c) The common bile ducts were carefully exposed and securely ligated on two occasions. (d) Following the procedure, sutures were applied and the area was thoroughly disinfected.

2.4. Immunofluorescent staining (IF)

Liver and small intestine tissues were embedded in paraffin, sectioned, dewaxed, and subjected to antigen retrieval through boiling in a citrate-EDTA antigen retrieval solution (P0086, Beyotime, China). The sections were washed thrice in PBS, blocked in immunol staining blocking buffer (P0102, Beyotime, China) for 1 h, and incubated with the primary antibody at room temperature. The primary antibodies used in this study were diluted as follows: NLRP3 (1:200, 27458-1-AP, Proteintech), F4/80 (1:200, 28463-1-AP-50, Proteintech), ZO-1 (1:500, GB111402, Servicebio), and CD31 (1:200, GB12063, Servicebio). After washing three times with PBS, the sections were incubated with the appropriate secondary antibodies at 37 °C for 1 h. The secondary antibodies used were goat anti-rabbit (Alexa Fluor 594 and Alexa Fluor 488) and goat anti-mouse (Alexa Fluor 594 and Alexa Fluor 488), all obtained from Beyotime. Following three washes in PBS, the nuclei were counterstained with DAPI. Subsequently, confocal immunofluorescence microscopy (Leica, USA) was employed to capture all IF images.

2.5. ELISA assay of the level of SIgA and LPS

The concentration of secretory immunoglobulin A (SIgA) in the intestinal mucosa was measured using a rat SIgA ELISA kit (CSB-E08412r, CUSABIO), while the concentration of LPS in the liver was evaluated using a rat LPS ELISA kit (CSB-E14247r, CUSABIO), following the instructions provided by the manufacturer.

2.6. The isolation of hepatocytes and Kupffer cells in liver

Hepatocytes and Kupffer cells in liver were isolated through collagenase digestion and differential centrifugation, following established protocols as previously described [24]. Subsequently, hepatocyte and Kupffer cells cocultures were simultaneously seeded, ensuring a consistent number of hepatocytes while adjusting the quantity of Kupffer cells to attain the desired ratios of hepatocytes to Kupffer cells.

2.7. Identification of Kupffer cells in liver

To identify Kupffer cells, the anti F4/80 antibody (1:200, Proteintech) was employed. Following incubation with the primary antibodies, the cells were rinsed with PBS and subsequently incubated with secondary antibodies (goat anti-rabbit IgG Alexa Fluor 488, Beyotime) for a duration of 1 h, while being shielded from light. Nuclei were counterstained with DAPI, and imaging was acquired using confocal microscopy (Olympus).

2.8. The collection of rat bile

Following the administration of anesthesia, the rats were subjected to weighing, followed by dissection of the abdomen. Subsequently, the common bile duct was cannulated in order to facilitate the collection of bile, as previously outlined [25].

2.9. Cell viability assay

MTT was used to determine cell viability. In detail, cells were seeded on 96-well plates at 1×10^4 cells/well. After treatment, cells were incubated with MTT for 2 h. To determine cell viability, the 96-well plate was read at 490 nm (reference 630 nm) for absorbance density values. Triplicates of all experiments were performed.

2.10. The quantification of ATP

ATP was quantified using a bioluminescence assay, employing an ATP Assay Kit (BC0305, Solarbio), in accordance with the instructions provided by the manufacturer. The term “extracellular ATP” refers to the concentration of ATP present in the culture medium of the cells.

2.11. RNA isolation and quantitative real-time PCR

The extraction of total RNA was conducted using Trizol reagent (Promega, USA), followed by cDNA synthesis using Eastep™ RT Master Mix (5X) (Promega, USA). Subsequently, qRT-PCR was carried out using GoTaq® qPCR Master Mix (Promega, USA) on a T100TM Thermal Cycler System (BioRad, USA). The relative expression of target gene was calculated using the $2^{-\Delta\Delta Ct}$ method. Fold change of target gene expression were calculated by normalization to the expression of the housekeeping gene GAPDH. And their sequences were as follows: NLRP3 (Forward: 5′- TCTGCATGCCGTATCTGGTT-3′ and Reverse: 5′- GGTACCCCATAGACTGGCAC-3′), caspase1 (Forward: 5′- GAACAAAGAAGGTGGCGCAT-3′ and Reverse: 5′- CAAGACGTGTACGAGTGGGT-3′), IL-18 (Forward: 5′- ACAGCCAACGAATCCCAGAC -3′ and Reverse: 5′- TCCATTTTGTTGTGTCCTGGC -3′), GSDMD (Forward: 5′- CTGACTCTTCGAGAACCGCT -3′ and Reverse: 5′- CTGACGGCATGATCCACGAT -3′), TLR4 (Forward: 5′- TAGCCATTGCTGCCAACATC -3′ and Reverse: 5′- ACACCAACGGCTCTGGATAA -3′), GAPDH (Forward: 5′- ACAGCAACAGGGTGGTGGAC -3′ and Reverse: 5′- TTTGAGGGTGCAGCGAACTT -3′).

2.12. Protein preparation and Western blot analysis

Tissues and cells were dissociated using cell lysis buffer containing protease inhibitors (Servicebio, China). Protein concentrations were measured using the BCA (Thermo Fisher Scientific, USA) method. The tissue and cell protein extracts were separated on SDS-PAGE gels and electro-transferred onto polyvinylidene fluoride membranes (Bio-Rad, USA). Specific proteins were detected using the following specific antibodies: Caspase-1 (1:2000, 22915-1-AP, Proteintech), Tubulin (1:2000,11224-1-AP, Proteintech), NLRP3 (1:2000, 27458-1-AP, Proteintech), IL-18 (1:2000,10663-1-AP, Proteintech), GSDMD (1:1000, 39754, CST) and β-actin (1:2000, 20536-1-AP, Proteintech). And incubation with anti-rabbit (1:5000, ab6721, Abcam) or anti-mouse (1:5000, ab6789, Abcam) secondary antibody for 1 h at 37 °C, the protein bands on the membranes were detected with the Odyssey infrared imaging system (LI-COR® Biosciences, USA) and analyzed according to the Odyssey software manual. All experiments were repeated at least three time.

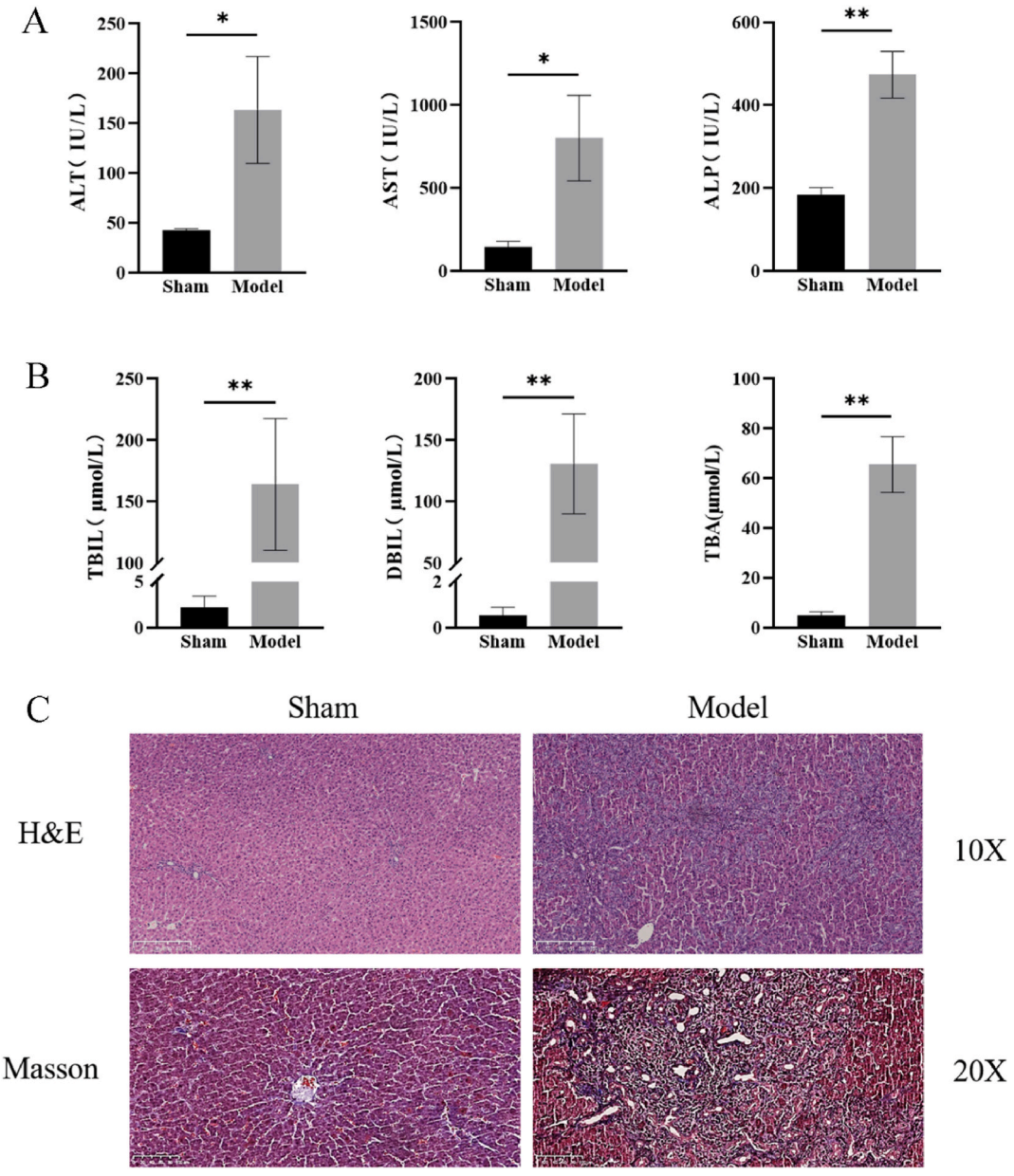

Fig. 2. The study evaluated liver injury resulting from BDL through the analysis of plasma and liver biochemistry, as well as liver morphology and histology. (A) The levels of serum ALT, AST, TBIL, DBIL, ALP, and TBA were measured. (B) The levels of serum TBIL, DBIL, and TBA were measured. (C) Representative images of rat liver histology analysis were obtained using H&E and Masson's Trichrome staining. *$p<0.05$, **$p<0.01$.

2.13. Statistical analysis

All the experimental data are presented as means ± standard deviations. Statistical significance was analyzed using one-way ANOVA, as appropriate, in SPSS 23.0 (USA). $p < 0.05$ was considered to statistical significance.

3. Results

3.1. Rats exhibit pronounced hepatic injury and fibrosis after BDL

Liver injury and cholestasis were evaluated through the measurement of ALT, AST (indicators of hepatocellular injury), and ALP (indicator of cholestasis) in serum samples [26]. The results revealed a statistically significant increase in ALP, ALT, and AST levels in the sera of rats subjected to BDL ($p<0.05$) (Fig. 2A), indicating acute liver injury and cholestasis in the model rats. Consistently, cholestasis in BDL rats was significantly more severe compared to sham rats, as evidenced by elevated levels of TBIL, DBIL, and TBA ($p<0.01$) (Fig. 2B). Histopathological analysis of liver tissues further corroborated these findings. As depicted in Fig. 2C, the liver tissues of sham group rats displayed a structurally intact appearance with well-organized hepatic cell cords. However, H&E staining of the liver tissues from the model group revealed significant alterations, including cellular enlargement, narrowing or absence of hepatic sinusoids, disorganization of the hepatic cord structure, hepatocyte edema, punctate necrosis, and infiltration of inflammatory cells

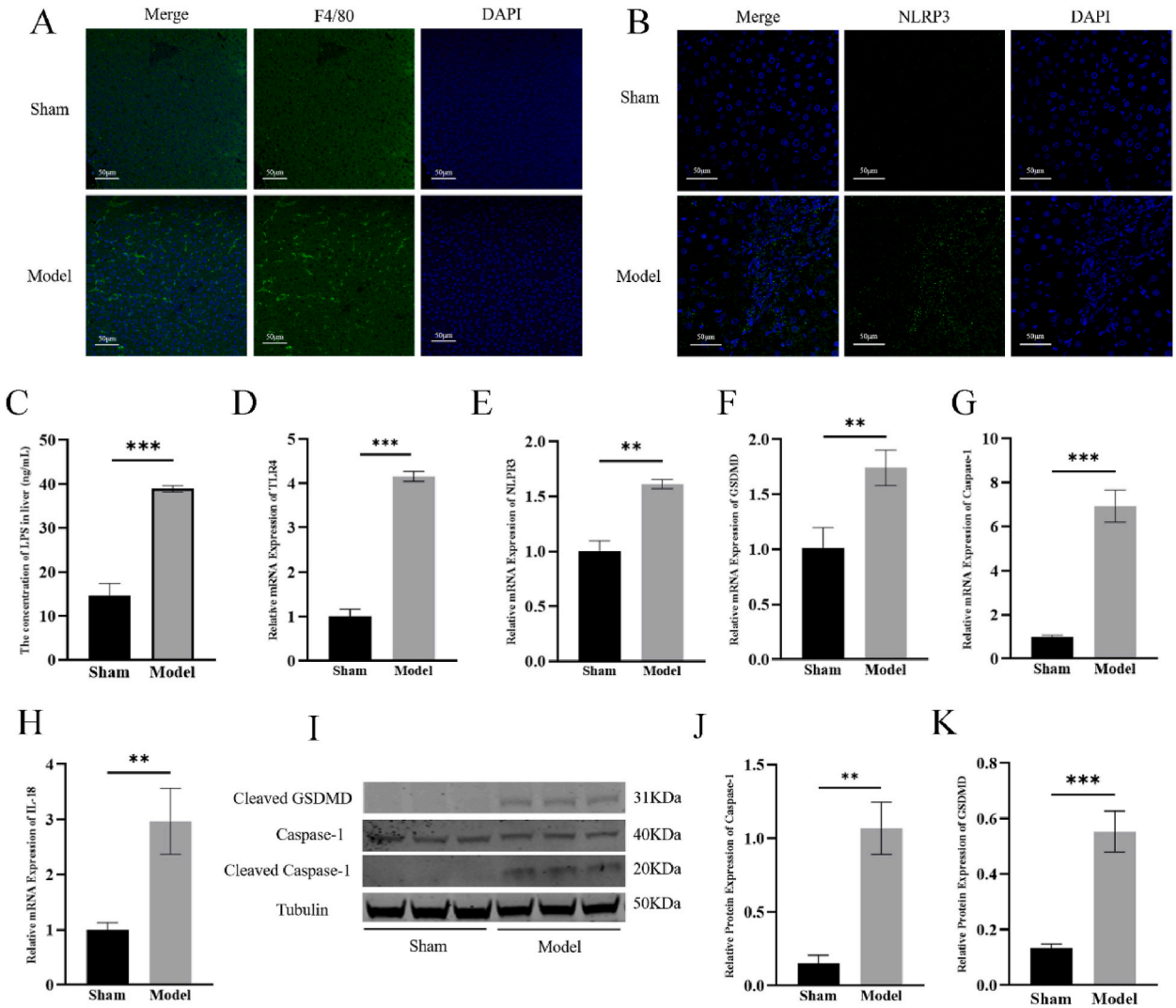

Fig. 3. The detection results of macrophages and inflammasomes activation markers. (A) Immunofluorescence analysis of F4/80. (B) Immunofluorescence analysis of NLRP3. (C) The ELISA was employed to determine the LPS concentration in the liver of rats. (D–H) The mRNA expression of TLR4, NLRP3, Caspase-1, IL-18 and GSDMD were determined by qRT-PCR analysis. (I–K) Western blot analysis of the protein expression of cleaved Caspase-1 and cleaved GSDMD. $^{**}p<0.01$, $^{***}p<0.001$.

(Fig. 2C). The Masson trichrome staining results were consistent with those obtained from the H&E staining. The model group exhibited the presence of blue stained fibrous tissue, which is indicative of notable liver fibrosis, liver lobular destruction, irregular hepatic cords, collagen fiber, hyperplasia, and an enlarged liver collagen area. (Fig. 2C).

3.2. After BDL, the activation of macrophages and inflammasomes leads to caspase-1-dependent pyroptosis

According to the findings depicted in Fig. 3A, macrophages (green) were specifically identified using an *anti*-F4/80 antibody. The model group exhibited a significantly elevated ratio of activated macrophages in comparison to the sham group. Similarly, the ratio of NLRP3 inflammasome (green), which is linked to the occurrence of pyroptosis [27], demonstrated a significant increase in BDL rats compared to the sham group (Fig. 3B). In comparison to the sham group, the ELISA assay revealed a significant increase in the presence of LPS ($p<0.001$), a component of gram-negative bacterial cell walls that activates macrophages through the TLR4 receptor [28,29], in

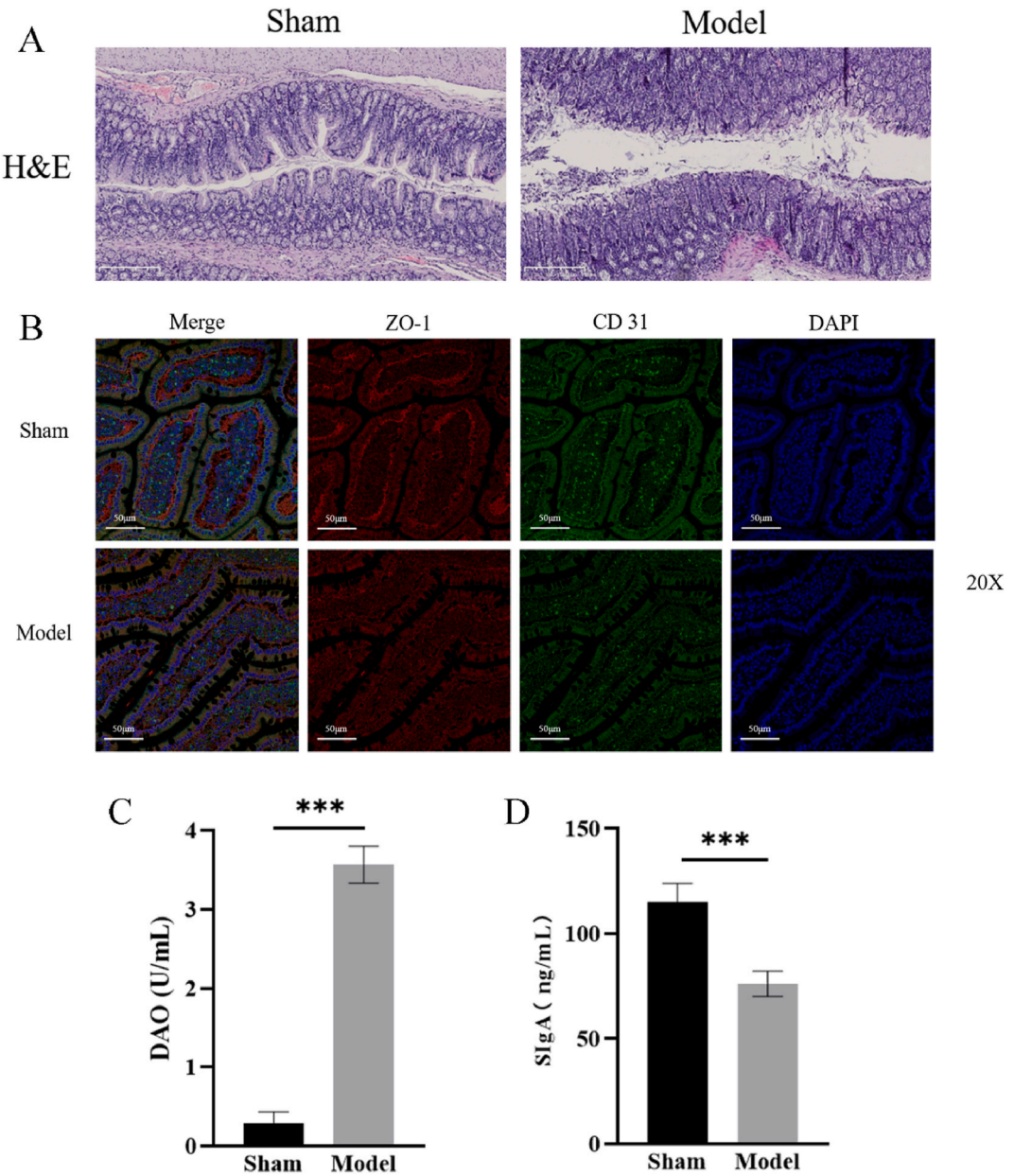

Fig. 4. The evaluation of intestinal barrier function in OJ rats. (A) Rat intestinal tissues were stained using the H&E staining. (B) The expression of ZO-1 (red) and CD 31 (green) was visualized through IF staining. (C) The activity of serum DAO. (D) The ELISA was employed to evaluate the levels of intestinal mucosa SIgA. ***$p<0.001$.

the model rats (Fig. 3C). Additionally, Fig. 3D demonstrates a noteworthy elevation in TLR4 mRNA expression, a crucial factor in LPS responsiveness [30], in the model group compared to the sham group ($p<0.001$). Subsequently, we examined the impact of BDL on the activation of markers associated with pyroptosis [31]. Following BDL, the mRNA levels of NLRP3, Caspase-1, IL-18, GSDMD, as well as the protein levels of cleaved Caspase-1 and cleaved GSDMD, were significantly upregulated compared to the sham group ($p<0.01$) (Fig. 3E–K).

3.3. The rats with OJ exhibit impaired intestinal barrier function

As depicted in Fig. 4A, the sham rats exhibited an intact intestinal mucosa characterized by well-arranged tall columnar epithelial cells. Conversely, the model rats displayed significant damage to the intestinal epithelium, including villous desquamation and infiltration of inflammatory cells, resulting in a noticeable loss of villus structure. Double-label immunofluorescence analysis indicated that, compared to sham rats, the co-localization of tight junction markers [32] (ZO-1) and the endothelial cell marker CD31 [33] was significantly diminished in model rats following BDL. This reduction in co-localization was attributed to the decreased ZO-1 immunoreactivity (Fig. 4B), implying substantial impairment of both the intestinal mechanical barrier and the vascular barrier [34]. Furthermore, measurements of plasma levels of DAO, which is positively correlated with intestinal permeability [35], and intestinal mucosa SIgA as indicators of intestinal mucosal injury [36], revealed that the levels of DAO and SIgA were significantly elevated in the model group compared to the sham group (Fig. 4C and D, $p<0.001$). These results suggest a substantial impairment in both the mechanical barrier and immune barrier functions of the intestines.

3.4. Relative abundance of gut microbiota changes at the phylum level

An examination of gut metagenomic diversity revealed notable disparities in the gut microbiota structures between the sham and model groups ($p < 0.05$), as evidenced by the principal coordinate analysis (PCoA) results (Fig. 5A). Specifically, at the phylum level, the sham group exhibited the presence of 16 distinct bacterial phyla, while the model group displayed 17. Notably, there were 14 shared species between the two groups (Fig. 5B). Furthermore, the Firmicutes (Gram-positive) phylum emerged as the predominant phylum in the sham group, constituting 84.02 % of the total, whereas in the model group, it accounted for 63.29 % (Fig. 5C). The Bacteroidota (Gram-negative) phylum exhibited the second highest dominance in both the sham and model groups, constituting 12.07 % in the sham group and 28.5 % in the model group (Fig. 5C). Furthermore, examination of species abundance disparities at the phylum level revealed a significant decrease in the abundance of Firmicutes in the model group compared to the sham group (Fig. 5D, E, $p < 0.01$). Conversely, the abundance of Bacteroidetes was found to be significantly higher in the model group as compared to the sham group (Fig. 5D–F, $p < 0.01$). These findings collectively indicate alterations in the population composition of Gram-positive and Gram-negative bacteria, with Firmicutes and Bacteroidetes being the predominant phyla for Gram-positive and Gram-negative bacteria, respectively.

3.5. Relative abundance of gut microbiota changes at the genus level

At the genus level, 246 different bacterial phyla were identified in sham group and 220 in model group, of these, 195 intersecting species (Fig. 6A). The relative abundance at the genus level displayed significant variation between the groups, as depicted in Fig. 6B. The predominant bacterial species in both the sham and model groups was Ruminococcaceae_UCG-005 (Gram-positive), constituting 19.52 % and 16.13 % of the total abundance, respectively. Compared to the sham group, the Ruminococcaceae_NK4A214_group (Gram-positive) exhibited a statistically significant decrease in abundance from 4.05 % to 2.72 %, as did the Lactobacillus (Gram-positive), which decreased significantly from 3.36 % to 0.29 %. Furthermore, the model group demonstrated a significant decline in the abundance of Ruminiclostridium_9 (Gram-positive) from 1.69 % to 0.97 % and Ruminiclostridium_5 (Gram-positive) from 1.62 % to 0.62 % when compared to the sham group. However, when compared to the sham rats, the model group exhibited a significant increase in the abundance of Bacteroides (Gram-negative), Escherichia-Shigella (Gram-negative), and Prevotella_1 (Gram-negative), with percentages rising from 2 % to 7.85 %, 0.04 %–3.28 %, and 0.09 %–1.44 % respectively. Furthermore, an analysis of species abundance at the genus level revealed that the abundance of Ruminococcaceae_NK4A214_group was significantly lower in the model group compared to the sham group (Fig. 6C and G, $p<0.05$). However, the abundance of Bacteroides, Prevotella_1, and Alloprevotella exhibited a statistically significant increase in the model group compared to the sham group (Fig. 6C–F, $p<0.05$). Consequently, at the genus level, there was a significant decrease in Gram-positive bacteria and a significant increase in Gram-negative bacteria in the model group relative to the sham group.

3.6. Hepatocytes and Kupffer cells were distinguished based on their morphological characteristics, and a cellular activity assay was conducted specifically for hepatocytes

The cells depicted in Fig. 7A displayed the characteristic polygonal morphology commonly observed in primary hepatocytes. Furthermore, the application of PAS staining revealed glycogen staining within the cytoplasm of the primary hepatocytes derived from rats. Additionally, IF staining using F4/80 was employed to identify Kupffer cells. As illustrated in Fig. 7B, IF assays demonstrated the localization of the Kupffer cells marker F4/80 within the cells (green), thereby confirming that the cells extracted corresponded to Kupffer cells. Subsequently, bile was collected from rats and diluted into various concentrations (10^{-1}, 10^{-2}, 10^{-3}, 10^{-4}, and 10^{-5}) using complete DMEM. Hepatocytes were then stimlated with these different concentrations of bile, and cells activity was assessed.

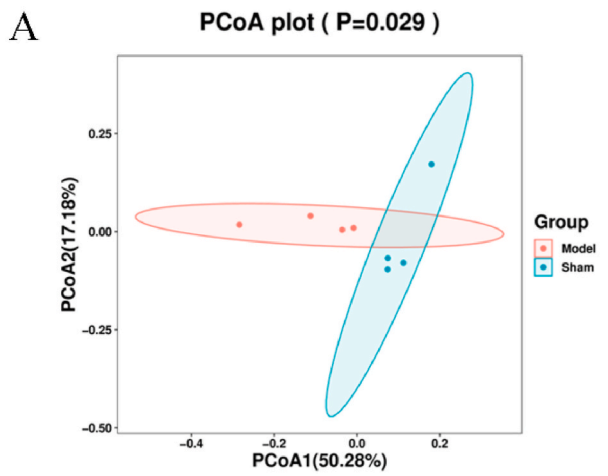

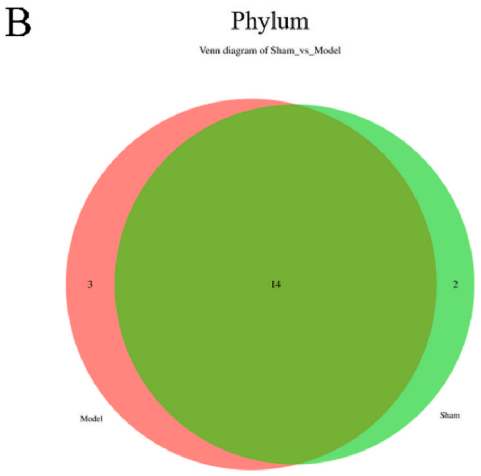

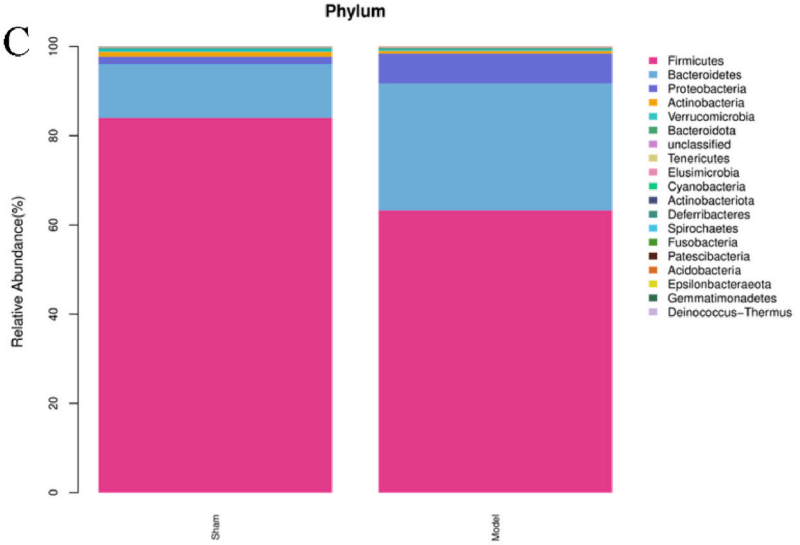

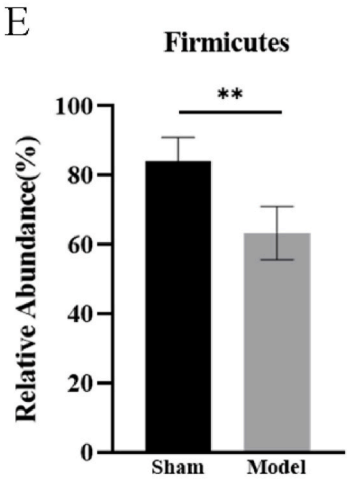

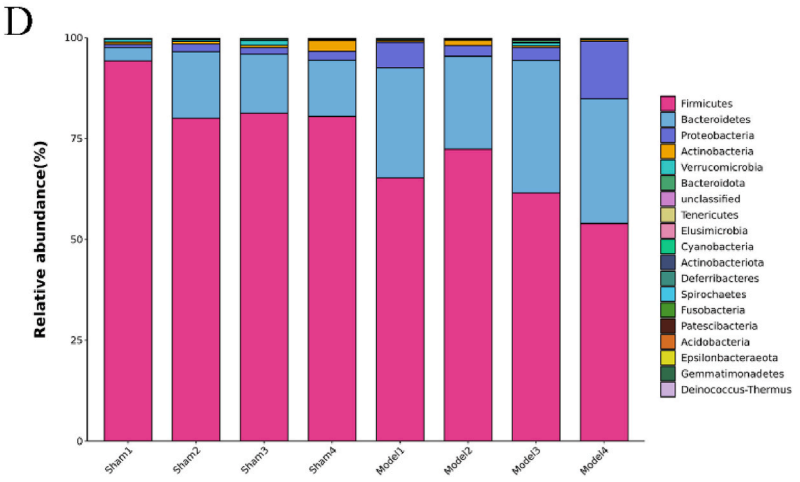

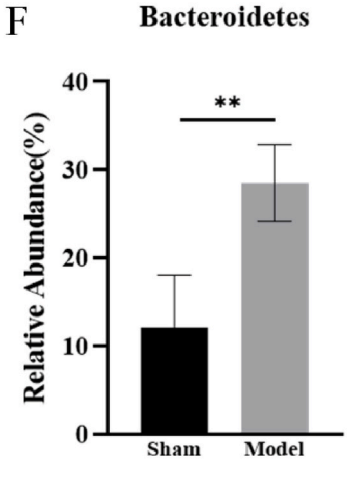

(caption on next page)

Fig. 5. The difference of species abundance at the phylum level between groups were analyzed by 16S rDNA sequencing. (A) The PCoA offers an overview of the alterations in the gut bacteriome of rats at the phylum level. (B) A Venn diagram is utilized to present statistical data on the horizontal microbial abundance at the phylum level. (C) The disparity in the relative abundance of gut bacteriome changes at the phylum level is observed between different groups. (D) The variation in the relative abundance of gut bacteriome changes at the phylum level is observed between different samples. (E) The abundance of the phylum Firmicutes is compared between different groups. (F) The abundance of the phylum Bacteroidetes is compared between different groups. $^{**}p<0.01$.

After a 24-h of bile treatment, it was observed that 10 % bile resulted in almost complete hepatocyte death, 1 % bile caused approximately 50 % hepatocyte death, while other concentrations did not cause significant damage to hepatocytes (Fig. 7C). Therefore, to investigate the impact of bile on hepatocytes, a concentration of 1 % bile was selected for subsequent research. Furthermore, hepatocytes were subjected to varying concentrations of LPS with 100 μg/mL, 10 μg/mL, 1 μg/mL, and 0.1 μg/mL. As depicted in Fig. 7D, the activity of hepatocytes remained unaffected after 24 h of LPS administration across the different concentrations used. Considering the aforementioned findings and existing literature [37], 1 μg/mL of LPS was chosen to stimulate hepatocytes in the subsequent experiment.

3.7. The concurrent occurrence of bile and LPS results in pronounced pyroptosis

As shown in Fig. 8A, following a 2-h exposure to bile treatment, the ATP concentration in the supernatant significantly increased in both the 10^{-1} and 10^{-2} groups when compared to the control group ($p<0.001$). The substantial release of ATP resulting from hepatocyte injury plays a crucial role in the initiation of pyroptosis in macrophages [38]. Furthermore, the activation of macrophages through LPS stimulation also contributes to the occurrence of pyroptosis [39]. Subsequently, in the context of hepatocyte and Kupffer cells co-culture, we employed bile and LPS stimulation to investigate the occurrence of pyroptosis. As depicted in Fig. 8B–F, the protein expression levels of NLRP3, cleaved GSDMD, IL-18 and cleaved Caspase-1 were significantly elevated in the LPS + Bile group compared to the control, LPS, and Bile groups ($p<0.01$). The mRNA expression levels of NLRP3, GSDMD, IL-18 and Caspase-1 were significantly elevated in the LPS + Bile group compared to other groups (Fig. 8G–J, $p<0.05$). Consequently, upon ATP stimulation, the Kupffer cells that were previously primed with LPS exhibited a pronounced pyroptotic response. Notably, the combined effect of LPS and bile was considerably more potent than the individual effects of LPS or bile alone.

4. Discussion

This study demonstrates that cholestasis induced by bile duct ligation (BDL) in rats leads to an imbalance in gut microbiota and compromises the intestinal barrier, allowing bacteria and lipopolysaccharide (LPS) to infiltrate liver tissue. We observed that obstructive jaundice (OJ) inflicted damage on liver cells, enhancing the expression of inflammasome components and pro-inflammatory cytokines within the liver. In vitro experiments revealed that direct exposure of bile acids to a co-culture of primary hepatocytes and Kupffer cells escalated ATP levels in supernatants and precipitated cell death. Notably, co-stimulation with LPS and ATP resulted in significantly increased inflammasome activation and pyroptotic cell death compared to stimulation with ATP alone.

Biochemical assays indicated elevated serum levels of ALP, ALT, AST, TBIL, DBIL, and TBA, marking acute liver injury and cholestasis in the rats (as illustrated in Fig. 2A and B). Histopathological examinations further revealed inflammation, widespread cell death, and fibrosis in the liver tissues (Fig. 2C). Immunofluorescence staining identified an increase in F4/80-positive cells, indicative of heightened Kupffer cell activity in the liver. Additionally, we noted a significant rise in the mRNA levels of TLR4, NLRP3, Caspase-1, IL-18, and GSDMD, as well as in the proteins of cleaved Caspase-1 and GSDMD in the BDL rats (Fig. 3). These findings support the hypothesis that inflammation-driven pyroptosis is a significant contributor to OJ-related liver damage, alongside direct cellular death mechanisms.

We corroborated prior findings that bile duct ligation (BDL) disrupts gut microbiota in rats, as evidenced by 16S rDNA sequencing analyses. Our investigations revealed that obstructive jaundice (OJ) notably increases the proportion of Gram-negative bacteria while decreasing Gram-positive bacteria at both the phylum and genus levels (Figs. 5 and 6). Consistent with existing literature, such microbial imbalances are known to compromise intestinal barriers, including mechanical [40], vascular [41], and immune components [42]. In our study, OJ significantly damaged the small intestine, manifesting as reduced expression of secretory immunoglobulin A (SIgA) in the intestinal mucosa, decreased zonula occludens-1 (ZO-1) protein levels, and elevated serum levels of diamine oxidase (DAO), indicative of increased intestinal permeability (Fig. 4). This compromise of the intestinal barrier facilitated the translocation of gut bacteria to the liver via the portal vein. Notably, we observed elevated levels of lipopolysaccharide (LPS) in the liver tissues of BDL rats, underscoring the hypothesis that gut microbiota dysbiosis exacerbates cholestatic liver injury by enabling bacterial translocation.

Pyroptosis is a form of programmed cell death initiated by various stimuli, including infections, toxins, molecular danger signals, or chemotherapy drugs [6,43]. This process predominantly affects immune cells like monocytes, macrophages, and dendritic cells [44]. Upon death, these cells release inflammatory mediators that recruit additional immune cells to the site of damage [43]. Kupffer cells, the resident macrophages of the liver, play a critical role in this process by detecting and binding to lipopolysaccharide (LPS), a component of bacterial cell walls, thereby responding to bacterial infections [45,46]. We hypothesized that cholestasis, a condition where bile flow is blocked, would cause liver cell death and release ATP, a molecule that signals danger. ATP would then activate inflammasomes, which are protein complexes that trigger pyroptosis. LPS, which increases due to bacterial translocation from the gut to the liver, would also activate pyroptosis in Kupffer cells and worsen liver injury. To investigate this, we established a co-culture

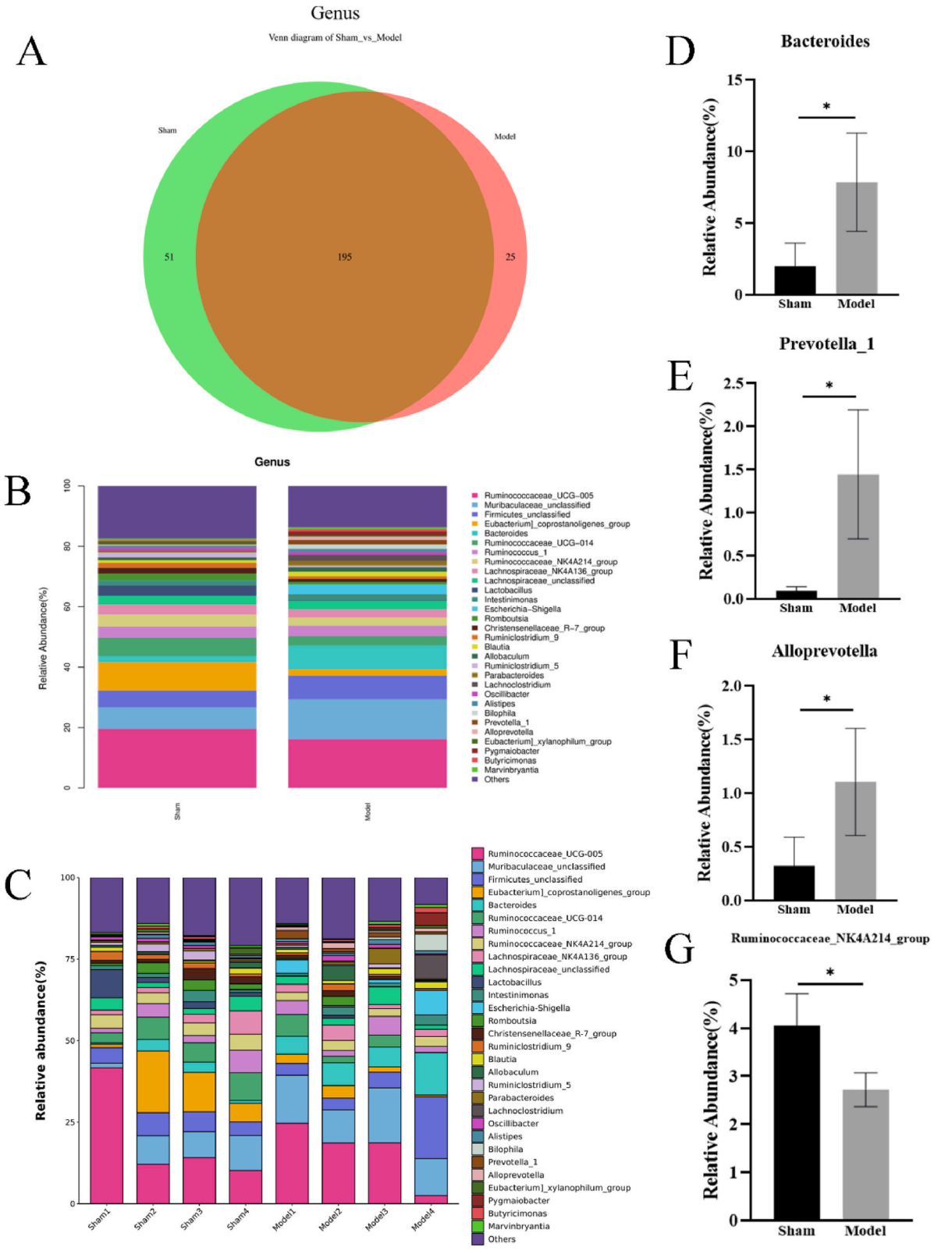

(caption on next page)

Fig. 6. The difference of species abundance at the genus level between groups were analyzed by 16S rDNA sequencing. (A) The statistical representation of horizontal microbial abundance at the genus level is presented by Venn diagram. (B) The variation in the relative abundance of gut bacteriome at the genus level differs between groups. (C) The variation in the relative abundance of gut bacteriome at the genus level differs between samples. (D) The abundance of Bacteroides differs between groups. (E) The abundance of Prevotella_1 differs between groups. (F) The abundance of Alloprevotella differs between groups. (G) The abundance of Ruminococcaceae_NK4A214_group differs between groups. *$p<0.05$.

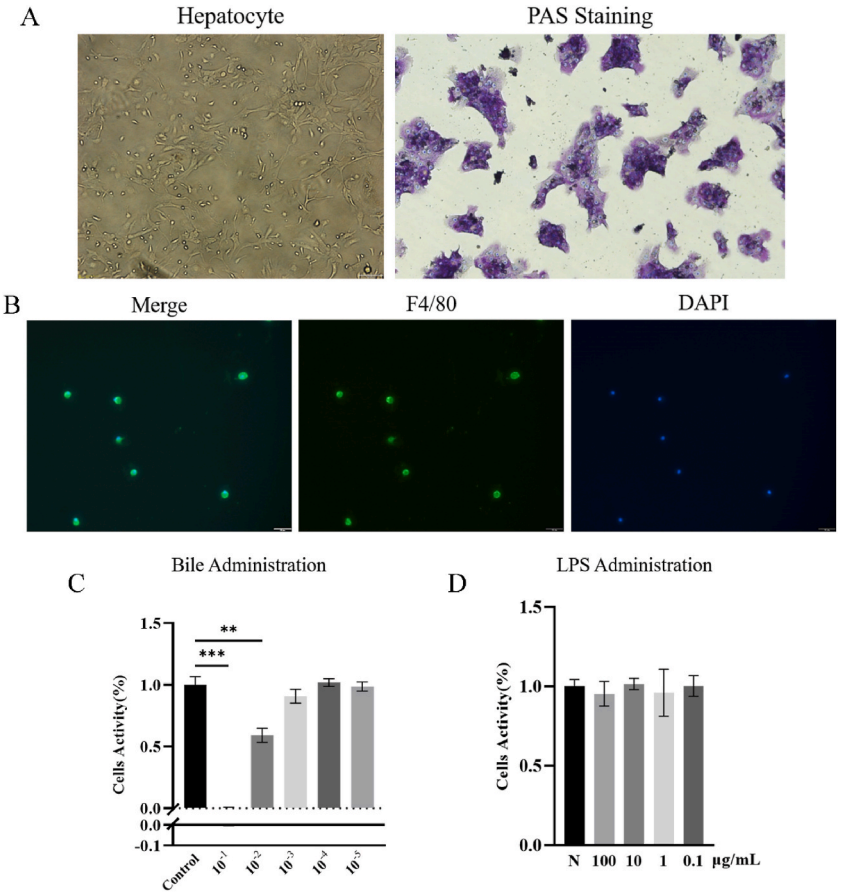

Fig. 7. The identification of hepatocytes and Kupffer cells, as well as the analysis of hepatocyte activity, were conducted. (A) Hepatocytes were identified based on their cellular morphology and positive staining with periodic acid-Schiff (PAS). (B) IF images were captured to visualize isolated Kupffer cells, which were identified by their positive expression of F4/80 (shown in green). (C) The activity of hepatocytes was analyzed following stimulation with bile. (D) The activity of hepatocytes was analyzed following stimulation with LPS. **$p<0.01$, ***$p<0.001$.

system of primary liver cells and Kupffer cells, treating them with either bile alone or in combination with LPS. We observed that bile exposure led to liver cell death and ATP release in a dose-dependent manner. Furthermore, this treatment triggered the formation and activation of the NLRP3 inflammasome, along with its downstream effectors (caspase-1, GSDMD, and IL-18) in Kupffer cells. The combination of bile and LPS significantly intensified Kupffer cell pyroptosis (Fig. 8). Our findings provide the first evidence that the synergistic effects of LPS and bile acids severely aggravate liver injury by promoting cell death and activating pyroptosis.

5. Conclusion

This study elucidates the contributory role of gut microbiota imbalance in exacerbating liver injury associated with obstructive jaundice. Specifically, disruptions in gut bacterial populations increase the hepatic concentration of LPS, a bacterial byproduct that triggers inflammatory responses. We demonstrated that the presence of bile, in conjunction with elevated LPS levels, precipitates pyroptosis, a pro-inflammatory form of cell death, primarily within Kupffer cells, the liver's resident immune cells. This interaction significantly intensifies liver damage through enhanced inflammatory activity and cellular destruction. These insights underscore the potential therapeutic value of targeting pyroptotic pathways to mitigate liver injury resultant from bile duct obstruction. Future research should, therefore, prioritize strategies that inhibit pyroptosis to ameliorate or prevent cholestasis-induced hepatic damage.

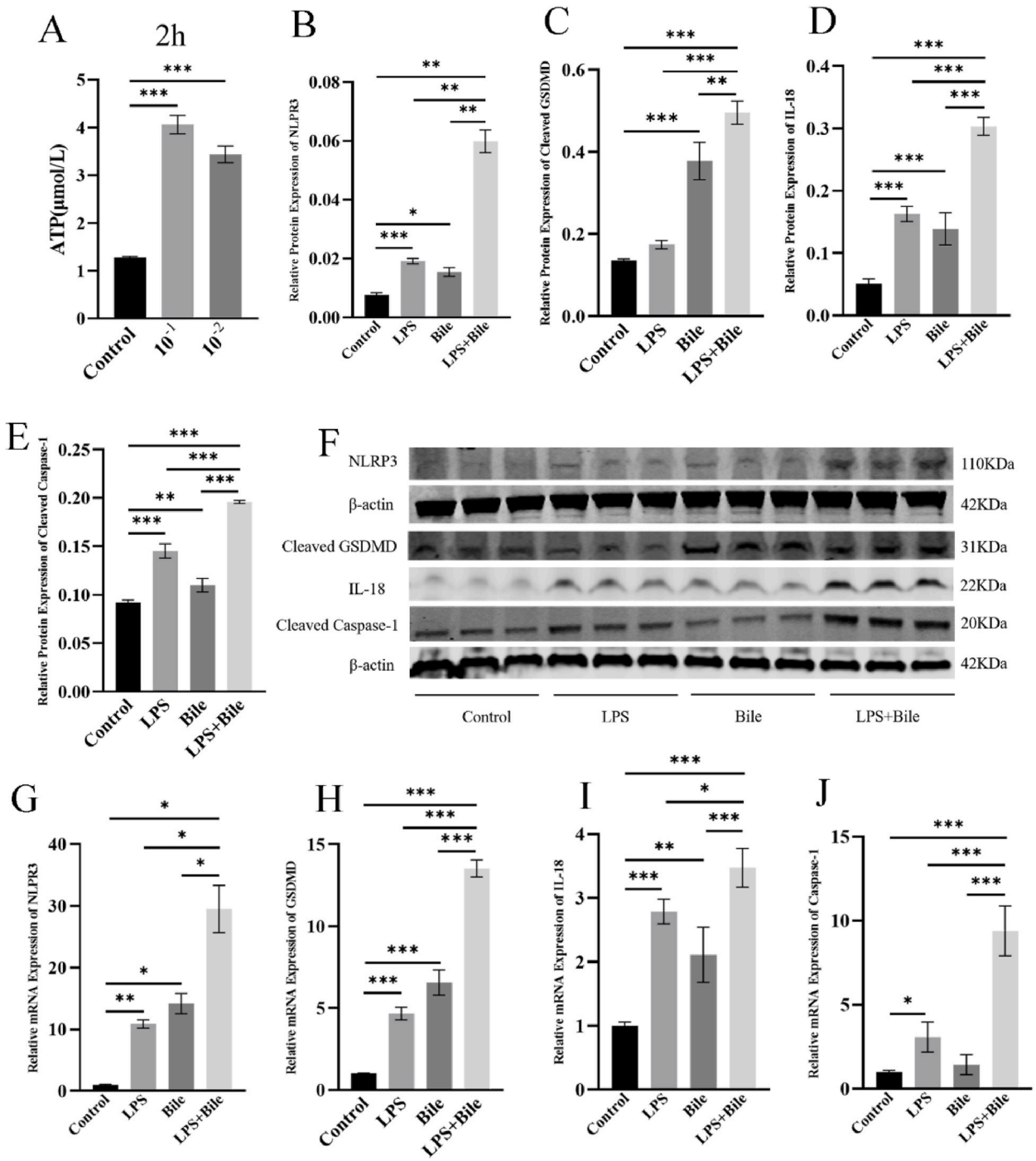

Fig. 8. Detection of ATP content and pyroptosis related biomarkers. (A) Detection of ATP content in the supernatant after bile stimulation of hepatocytes. 10^{-1} group: Rat bile diluted 10 times by complete DMEM. 10^{-2} group: Rat bile diluted 100 times by complete DMEM. (B–F) The protein expression of NLRP3, cleaved GSDMD, IL-18 and cleaved Caspase-1 were detected by Western blot. (G–J) The mRNA expression of NLRP3, GSDMD, IL-18 and Caspase-1 were detected by qPCR. Cell species: Hepatocyte and Kupffer cells co-culture. Control: Complete DMEM; LPS: Complete DMEM+1 μg/mL LPS; Bile: Complete DMEM+10^{-2} bile; LPS + Bile: Complete DMEM+1 μg/mL LPS+10^{-2} bile. *$p<0.05$, **$p<0.01$, ***$p<0.001$.

Funding information

This work was supported by Heilongjiang Province Traditional Chinese Medicine Research Project (grant number ZHY2020-065).

Ethics statement

All experimental procedures and animal handling were performed with the approval of the Animal Care and Use Committee of Medical Research Institute of Yiling (NO. N2022014), in accordance with the National Institutes of Health Guide for the Care and Use of Laboratory Animals. And all research was conducted in accordance with both the Declarations of Helsinki and Istanbul.

Data availability statement

Most of the data are available in all Tables and Figures of the manuscripts. Moreover, the data will available on request.

CRediT authorship contribution statement

Xin Shen: Writing – original draft, Supervision, Project administration, Investigation. **Xin Zhang:** Writing – original draft, Project administration, Methodology, Data curation, Conceptualization. **Kaiyu Li:** Resources, Methodology, Investigation. **Guangming Huang:** Formal analysis, Data curation, Conceptualization. **Xinyu Li:** Resources, Project administration, Methodology, Investigation. **Yunlong Hou:** Writing – review & editing, Supervision, Project administration, Conceptualization. **Xin Ge:** Writing – review & editing, Supervision, Funding acquisition, Conceptualization.

Declaration of generative AI and AI-assisted technologies in the writing process

AI was not used during the writing process of this article.

Declaration of competing interest

The authors declare that the research was conducted in the absence of any commercial or financial relationships that could be construed as a potential conflict of interest.

Acknowledgements

Assistance with the study: G.X., and H.-Y.L. design the experiments; S.X., and Z.X. performed the experiments; L.-K.Y., H.-G.M., and L.-X.Y. analyzed and interpreted the data; S.X., Z.X., and H.-Y.L. wrote the manuscript. All authors discussed the results and commented on the manuscript.

References

[1] H.Q. Wang, X.Y. Meng, J.M. Zhang, J.Y. Chen, B.H. Zhang, F.X. Wu, Alterations of actin cytoskeleton and arterial protein level in patients with obstructive jaundice, Genet. Mol. Biol. 45 (3) (2022) e20210419.
[2] C. Wang, Y. Xu, X. Lu, Should preoperative biliary drainage be routinely performed for obstructive jaundice with resectable tumor, Hepatobiliary Surg. Nutr. 2 (5) (2013) 266–271.
[3] S. Wei, X. Ma, Y. Zhao, Mechanism of hydrophobic bile acid-induced hepatocyte injury and drug discovery, Front. Pharmacol. 11 (2020) 1084.
[4] Y. Xiao, Y. Zhou, Y. Lu, K. Zhou, W. Cai, PHB2 interacts with LC3 and SQSTM1 is required for bile acids-induced mitophagy in cholestatic liver, Cell Death Dis. 9 (2) (2018) 160.
[5] T. Bergsbaken, S.L. Fink, B.T. Cookson, Pyroptosis: host cell death and inflammation, Nat. Rev. Microbiol. 7 (2) (2009) 99–109.
[6] Y. Wang, H. Zhang, Q. Chen, et al., TNF-α/HMGB1 inflammation signalling pathway regulates pyroptosis during liver failure and acute kidney injury, Cell Prolif. 53 (6) (2020) e12829.
[7] Z. Li, H. Xu, X. Liu, et al., GDF11 inhibits cardiomyocyte pyroptosis and exerts cardioprotection in acute myocardial infarction mice by upregulation of transcription factor HOXA3, Cell Death Dis. 11 (10) (2020) 917.
[8] C. Gabay, C. Lamacchia, G. Palmer, IL-1 pathways in inflammation and human diseases, Nat. Rev. Rheumatol. 6 (4) (2010) 232–241.
[9] X.P. Wang, W.C. Zheng, Y. Bai, et al., Carbon monoxide-releasing molecule-3 alleviates kupffer cell pyroptosis induced by hemorrhagic shock and resuscitation via sGC-cGMP signal pathway, Inflammation 44 (4) (2021) 1330–1344.
[10] G. Fan, Y. Li, J. Chen, Y. Zong, X. Yang, DHA/AA alleviates LPS-induced Kupffer cells pyroptosis via GPR120 interaction with NLRP3 to inhibit inflammasome complexes assembly, Cell Death Dis. 12 (1) (2021) 73.
[11] T.D. Leser, L. Mølbak, Better living through microbial action: the benefits of the mammalian gastrointestinal microbiota on the host, Environ. Microbiol. 11 (9) (2009) 2194–2206.
[12] F. Vasaï, K.B. Ricaud, L. Cauquil, et al., Lactobacillus sakei modulates mule duck microbiota in ileum and ceca during overfeeding, Poult Sci 93 (4) (2014) 916–925.
[13] S.A. Whiteside, H. Razvi, S. Dave, G. Reid, J.P. Burton, The microbiome of the urinary tract–a role beyond infection, Nat. Rev. Urol. 12 (2) (2015) 81–90.
[14] K.M. Burkholder, K.L. Thompson, M.E. Einstein, T.J. Applegate, J.A. Patterson, Influence of stressors on normal intestinal microbiota, intestinal morphology, and susceptibility to Salmonella enteritidis colonization in broilers, Poult Sci 87 (9) (2008) 1734–1741.
[15] P. Zhang, J. Liu, B. Xiong, et al., Microbiota from alginate oligosaccharide-dosed mice successfully mitigated small intestinal mucositis, Microbiome 8 (1) (2020) 112.
[16] S.M. Shin, J.H. Yang, S.H. Ki, Role of the Nrf2-ARE pathway in liver diseases, Oxid. Med. Cell. Longev. 2013 (2013) 763257.

[17] R.W. Parks, C.H. Stuart Cameron, C.D. Gannon, C. Pope, T. Diamond, B.J. Rowlands, Changes in gastrointestinal morphology associated with obstructive jaundice, J. Pathol. 192 (4) (2000) 526–532.
[18] C.D. Scopa, S. Koureleas, A.C. Tsamandas, et al., Beneficial effects of growth hormone and insulin-like growth factor I on intestinal bacterial translocation, endotoxemia, and apoptosis in experimentally jaundiced rats, J. Am. Coll. Surg. 190 (4) (2000) 423–431.
[19] S.F. Assimakopoulos, C.E. Vagianos, N. Patsoukis, C. Georgiou, V. Nikolopoulou, C.D. Scopa, Evidence for intestinal oxidative stress in obstructive jaundice-induced gut barrier dysfunction in rats, Acta Physiol. Scand. 180 (2) (2004) 177–185.
[20] R. Liu, X. Li, Z. Huang, et al., C/EBP homologous protein-induced loss of intestinal epithelial stemness contributes to bile duct ligation-induced cholestatic liver injury in mice, Hepatology 67 (4) (2018) 1441–1457.
[21] O. Chazouillères, Novel aspects in the management of cholestatic liver diseases, Dig. Dis. 34 (4) (2016) 340–346.
[22] S.F. Assimakopoulos, C.D. Scopa, G. Zervoudakis, et al., Bombesin and neurotensin reduce endotoxemia, intestinal oxidative stress, and apoptosis in experimental obstructive jaundice, Ann. Surg. 241 (1) (2005) 159–167.
[23] A. Brandoni, A.M. Torres, Expression of renal Oat5 and NaDC1 transporters in rats with acute biliary obstruction, World J. Gastroenterol. 21 (29) (2015) 8817–8825.
[24] M. Froh, A. Konno, R.G. Thurman, Isolation of liver Kupffer cells, Curr Protoc Toxicol (2003) (Chapter 14): Unit14.4.
[25] J. Tu, Q. Li, B. Zhou, The tannins from sanguisorba officinalis L. (rosaceae): a systematic study on the metabolites of rats based on HPLC-LTQ-orbitrap MS(2) analysis, Molecules 26 (13) (2021) 4053.
[26] V.L. Chen, X. Du, Y. Chen, et al., Genome-wide association study of serum liver enzymes implicates diverse metabolic and liver pathology, Nat. Commun. 12 (1) (2021) 816.
[27] O. Dufies, A. Doye, J. Courjon, et al., Escherichia coli Rho GTPase-activating toxin CNF1 mediates NLRP3 inflammasome activation via p21-activated kinases-1/2 during bacteraemia in mice, Nat Microbiol 6 (3) (2021) 401–412.
[28] L. Guery, N. Benikhlef, T. Gautier, et al., Fine-tuning nucleophosmin in macrophage differentiation and activation, Blood 118 (17) (2011) 4694–4704.
[29] A. Hulina, M. Grdić Rajković, D. Jakšić Despot, et al., Extracellular Hsp70 induces inflammation and modulates LPS/LTA-stimulated inflammatory response in THP-1 cells, Cell Stress Chaperones 23 (3) (2018) 373–384.
[30] E.A. Ra, T.A. Lee, Kim S. Won, et al., TRIM31 promotes Atg5/Atg7-independent autophagy in intestinal cells, Nat. Commun. 7 (2016) 11726.
[31] Z. Xue, Q. Xi, H. Liu, et al., miR-21 promotes NLRP3 inflammasome activation to mediate pyroptosis and endotoxic shock, Cell Death Dis. 10 (6) (2019) 461.
[32] G. Xu, Y. Li, C. Ma, et al., Restraint stress induced hyperpermeability and damage of the blood-brain barrier in the amygdala of adult rats, Front. Mol. Neurosci. 12 (2019) 32.
[33] S. Wang, M. Xu, F. Li, et al., Ethanol promotes mammary tumor growth and angiogenesis: the involvement of chemoattractant factor MCP-1, Breast Cancer Res. Treat. 133 (3) (2012) 1037–1048.
[34] M. Ramirez-Pedraza, M. Fernández, Interplay between macrophages and angiogenesis: a double-edged sword in liver disease, Front. Immunol. 10 (2019) 2882.
[35] S. Lu, S. Xu, L. Chen, Y. Deng, J. Feng, Periplaneta americana extract pretreatment alleviates oxidative stress and inflammation and increases the abundance of gut akkermansia muciniphila in diquat-induced mice, Antioxidants 11 (9) (2022) 1806.
[36] Z. Deng, X.M. Luo, J. Liu, H. Wang, Quorum sensing, biofilm, and intestinal mucosal barrier: involvement the role of probiotic, Front. Cell. Infect. Microbiol. 10 (2020) 538077.
[37] K.A. Mcdonald, H. Huang, S. Tohme, et al., Toll-like receptor 4 (TLR4) antagonist eritoran tetrasodium attenuates liver ischemia and reperfusion injury through inhibition of high-mobility group box protein B1 (HMGB1) signaling, Mol. Med. 20 (1) (2015) 639–648.
[38] S. Mariathasan, D.S. Weiss, K. Newton, et al., Cryopyrin activates the inflammasome in response to toxins and ATP, Nature 440 (7081) (2006) 228–232.
[39] J. Chen, X. Deng, Y. Liu, et al., Kupffer cells in non-alcoholic fatty liver disease: friend or foe, Int. J. Biol. Sci. 16 (13) (2020) 2367–2378.
[40] Y.J. Sun, W.M. Chen, T.Z. Zhang, H.J. Cao, J. Zhou, Effects of cardiopulmonary bypass on tight junction protein expressions in intestinal mucosa of rats, World J. Gastroenterol. 14 (38) (2008) 5868–5875.
[41] K. Jadhav, T.S. Cohen, Can you trust your gut? Implicating a disrupted intestinal microbiome in the progression of NAFLD/NASH, Front. Endocrinol. 11 (2020) 592157.
[42] H. Turula, J. Bragazzi Cunha, B.A. Mainou, et al., Natural secretory immunoglobulins promote enteric viral infections, J. Virol. 92 (23) (2018) e00826-18.
[43] J. Wu, S. Lin, B. Wan, B. Velani, Y. Zhu, Pyroptosis in liver disease: new insights into disease mechanisms, Aging Dis 10 (5) (2019) 1094–1108.
[44] E.A. Miao, J.V. Rajan, A. Aderem, Caspase-1-induced pyroptotic cell death, Immunol. Rev. 243 (1) (2011) 206–214.
[45] M. Jacques, J. Labrie, F. St Michael, et al., Isolation of an atypical strain of Actinobacillus pleuropneumoniae serotype 1 with a truncated lipopolysaccharide outer core and no O-antigen, J. Clin. Microbiol. 43 (7) (2005) 3522–3525.
[46] I. Nagaoka, S. Hirota, F. Niyonsaba, M. Hirata, Y. Adachi, H ea Tamura, Cathelicidin family of antibacterial peptides CAP18 and CAP11 inhibit the expression of TNF-alpha by blocking the binding of LPS to CD14(+) cells, J. Immunol. 167 (6) (2001) 3329–3338.